

Engineering Interlayer Hybridization in Energy Space via Dipolar Overlayers

Bin Shao^{1,2}, Xiao Jiang², Jan Berges³, Sheng Meng^{4,5,6}, Bing Huang^{2,7*}

1. College of Electronic Information and Optical Engineering, Nankai University, Tianjin 300350, China
2. Beijing Computational Science Research Center, Beijing 100193, China
3. Institut für Theoretische Physik, Bremen Center for Computational Materials Science, and MAPEX Center for Materials and Processes, Universität Bremen, Bremen D-28359, Germany
4. Beijing National Laboratory for Condensed Matter Physics and Institute of Physics, Chinese Academy of Sciences, Beijing 100190, China
5. Songshan Lake Materials Laboratory, Dongguan, Guangdong 523808, China
6. School of Physical Sciences, University of Chinese Academy of Sciences, Beijing 100049, China
7. Department of Physics, Beijing Normal University, Beijing 100875, China

E-mail: bing.huang@csrc.ac.cn

The interlayer hybridization (IH) of van der Waals (vdW) materials is thought to be mostly associated with the unignorable interlayer overlaps of wavefunctions (t) in real space. Here, we develop a more fundamental understanding of IH by introducing a new physical quantity, the IH admixture ratio α . Consequently, an exotic strategy of IH engineering in energy space can be proposed, i.e., instead of changing t as commonly used, α can be effectively tuned in energy space by changing the onsite energy difference (2Δ) between neighboring-layer states. In practice, this is feasible via reshaping the electrostatic potential of the surface by depositing a dipolar overlayer, e.g., crystalline ice. Our first-principles calculations unveil that IH engineering via adjusting 2Δ can greatly tune interlayer optical transitions in transition-metal dichalcogenide bilayers, switch different types of Dirac surface states in Bi_2Se_3 thin films, and control magnetic phase transition of charge density waves in 1H/1T-TaS₂ bilayers, opening new opportunities to govern the fundamental optoelectronic, topological, and magnetic properties of vdW systems beyond the traditional interlayer-distance or twisting engineering.

The interlayer hybridization (IH) of stacked two-dimensional (2D) van der Waals (vdW) materials manifests itself as a unique tuning knob for their overall physical properties¹⁻⁶. Compared with the conventional bulk materials, this hybridization arises from the relatively weak vdW interaction, whose strength is comparable to that of external stimuli. Therefore, (i) it can be lifted by mechanical exfoliation⁷, opening the door for atomically thin 2D materials; (ii) it can also be utilized to manipulate the electronic properties of vdW homo/hetero-structures, not only to engineer their band structures^{3,8}, but also to drive a variety of many-body phenomena such as magnetic phase transitions^{9,10}, superconductivity¹¹, interlayer excitons^{5,12,13}, and charge density waves (CDWs)^{14,15}; (iii) it can even be applied to realize twist engineering, bringing the studies of superconducting¹⁶ or strongly correlated phases¹⁷ in the 2D limit to a new level. Thus, searching an efficient way of tuning the IH always plays a central role for both fundamental studies and practical applications of stacked vdW materials.

In general, the electronic states of each monolayer component in vdW-stacked systems can be considered as states confined in a vertical finite-depth quantum well. As demonstrated in Fig. 1a (upper panel), the states in each well cannot be fully confined, leading to unignorable overlap of their wavefunctions in real space, referred to as t , between the quantum wells of different layers. Usually, the IH is tacitly accepted to be mostly associated with t , whose value can be effectively tuned in real space by mechanical exfoliation⁷, stacking modulation^{14,15}, and twisting^{16,17}, resulting in scientific (i)-(iii) discoveries discussed above. A fundamental question is raised here: Besides tuning t as commonly used, is there an alternative way to tune the IH? The answer to this question relies on a more fundamental understanding of the IH.

In addition to t in real space, as shown in the Fig. 1a (bottom panel), there can be an offset energy, referring as 2Δ , in the onsite energy of neighboring-layer states in energy space. Similar to real-space t , this 2Δ can be understood as the energy-space “overlap” of the coupled states. Considering these two overlaps and summarizing all the k -dependence of the initial energy dispersion in $\varepsilon_0(k)$, the IH can be illustrated in a minimal two-band model involving states $|a\rangle = (1,0)$ and $|b\rangle = (0,1)$ belonging to the A and B layer, respectively. The resulting Hamiltonian reads $\hat{H}(k) = \varepsilon_0(k)\mathbf{1} + t\sigma_1 - \Delta\sigma_3$, where the σ_i refer to the Pauli matrices. The eigenstates of the Hamiltonian are $|+\rangle = \cos(\varphi)|b\rangle + \sin(\varphi)|a\rangle$ and $|-\rangle = \cos(\varphi)|a\rangle - \sin(\varphi)|b\rangle$, respectively, with $\tan 2\varphi = t/\Delta$ and corresponding energies $\varepsilon_{\pm}(k) = \varepsilon_0(k) \mp \sqrt{\Delta^2 + t^2}$. The IH yields an admixture of the wavefunctions of $|a\rangle$ and $|b\rangle$. To describe the degree of this admixture, we define a key physical quantity, the IH admixture ratio α , as the difference of the eigenstates’ weights on $|a\rangle$ and $|b\rangle$, which reads $\alpha = 1 - \frac{|\langle \pm | a \rangle \langle a | \pm \rangle - \langle \pm | b \rangle \langle b | \pm \rangle|}{|\langle \pm | a \rangle \langle a | \pm \rangle + \langle \pm | b \rangle \langle b | \pm \rangle} = 1 - 1/\sqrt{1 + 4(t/2\Delta)^2}$ with $t/2\Delta \in [0, +\infty]$. Importantly, the α unveils a more fundamental understanding of the IH, i.e., the IH is instead prone to the ratio of the two overlaps $t/2\Delta$, not merely related to t as generally accepted.

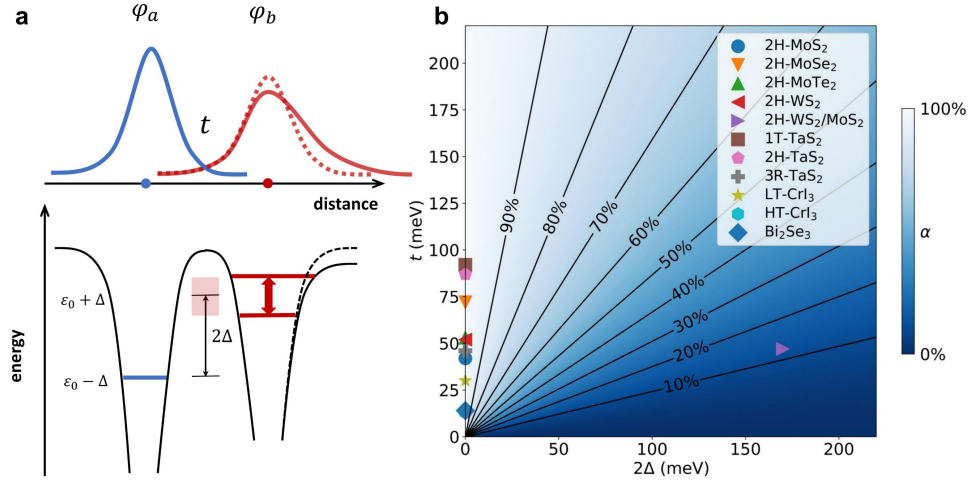


Fig.1 IH engineering in stacked vdW systems. (a) Schematic diagram of the interlayer hybridization (IH) in real space (upper panel) and energy space (bottom panel). Reshaping the electrostatic potential, denoted as dashed lines, leads to the variation of the onsite energy of layer B, along with the change of onsite energy difference 2Δ between neighboring layers. (b) Phase diagram of the IH admixture ratio α as a function of t and 2Δ , where the calculated α of several commonly used 2D systems are also indicated.

The phase diagram of α as a function of t and 2Δ is depicted in Fig. 1b, where the two parameters of several commonly used homo/hetero-structures are also shown (see full data in Supplemental Table 1). For homo-structures, $2\Delta = 0$, resulting in the highest admixture ratio $\alpha = 100\%$ of electronic states between neighboring layers. In contrast, the $2\Delta \neq 0$ in hetero-structures, thus, the corresponding α can be relatively small, e.g., $2\Delta = 200$ meV results in $\alpha = 12.5\%$ in 2H-MoS₂/WS₂. Interestingly, the phase diagram strongly indicates that even without changing t , the α of vdW systems can still be effectively weakened or enhanced by varying 2Δ . As shown in Fig. 1a, we propose that tuning 2Δ is feasible via asymmetrically reshaping the electrostatic potential of the stacked 2D systems, e.g., via depositing a dipole overlayer on the top or bottom surface, providing an alternative opportunity for IH engineering in energy space.

Crystalline ice, exhibiting the hexagonal Ih phase (Ih-ice) under a normal pressure¹⁸, is one of the most common dipole layers existing in nature. Here, we propose to engineer α via modulating 2Δ instead of t , which can be achieved by depositing an Ih-ice overlayer on the upper surface of 2D vdW systems. Using first-principles calculations, we demonstrate that IH engineering via tuning 2Δ can realize greatly tunable interlayer optical transitions in transition-metal dichalcogenide (TMD) bilayers, switchable different types of Dirac surface states in Bi₂Se₃ thin films, and controllable magnetic phase transition of CDW in 1H/1T-TaS₂ hetero-bilayers, which potentially opens a new door to engineer the optoelectronic, topological, and magnetic properties of 2D vdW systems.

Case I: Tunable interlayer optical transitions in TMD bilayers

Band-edge optical transitions (BOTs) play a central role in determining the fundamental optoelectronic properties of semiconductors. In general, there are two types of BOTs in layered materials, i.e., interlayer BOTs and intralayer BOTs. In practice, it is interesting to realize a highly

tunable interlayer BOT, that is fundamentally related to the magnitude of interlayer optical transition probabilities (r^2 , squares of transition dipole moments) between the band-edge states, for controllable interlayer exciton and lighting^{6,19}. Usually, the interlayer r^2 are the intrinsic properties of a system, which strongly depend on α . Taking TMD bilayers as examples, as shown in Fig. 2a, the smaller (larger) α in the hetero-bilayer (homo-bilayer) indicates a weaker (stronger) IH admixture between different layers, which may consequently result in a weaker (stronger) interlayer r^2 . Here, we propose that via 2Δ engineering – tuning IH by changing 2Δ – we may greatly tune $r^2(\alpha)$ in TMD bilayers.

To verify this idea, we construct a supercell with a $\sqrt{3} \times \sqrt{3}$ Ih-ice overlayer on a $\sqrt{7} \times \sqrt{7}$ TMD bilayer (see Supplemental Figs. 1 and 2) to minimize the lattice mismatch between them. First, we consider the hetero-bilayer WS₂/MoS₂. The calculated $2\Delta = 169$ meV gives rise to a small $\alpha = 12.5\%$ in WS₂/MoS₂. Fig. 2b shows the calculated unfolded orbital-resolved effective band structure of AB-stacked WS₂/MoS₂. Overall, the band-edge states in WS₂/MoS₂ exhibit a type-II band alignment. Interestingly, depositing a double-layer (2L) Ih-ice on top of WS₂/MoS₂ (Fig. 2c) effectively reduces 2Δ from 169 to 57 meV, leading to a large enhancement of α from 12.5% to 47.9%. More importantly, although the band structures before and after Ih-ice deposition are very similar, the interlayer r^2 is significantly enhanced (Fig. 2g) with respect to the ice-free (0L) case (Fig. 2f), consistent with the mechanism proposed in Fig. 2a.

Second, we consider the homo-bilayer MoS₂/MoS₂. Since $2\Delta = 0$ in MoS₂/MoS₂ (Fig. 2d), $\alpha = 100\%$, leading to the electronic states from different MoS₂ layers being energetically degenerated. The $\alpha = 100\%$ in MoS₂/MoS₂ induces large band splittings around the Γ point in the top of the valence band (VB) and along the paths Γ -K/ Γ -M in the bottom of the conduction band (CB), which are absent in monolayer MoS₂ (see Supplemental Fig. 3). The situation is dramatically changed when a 2L Ih-ice is deposited on top of MoS₂/MoS₂. As shown in Fig. 2e, the bands from different layers are rigidly shifted with respect to each other, forming an ideal type-II band alignment. The calculated $2\Delta = 222$ meV gives rise to a dramatic reduction of α from 100% to 7.6%. This rather small α can not only effectively eliminate the original band splitting in the ice-free (0L) case (Fig. 2d), but can also convert the band structure of the top MoS₂ layer in MoS₂/MoS₂ from indirect bandgap to direct bandgap, similar to that of monolayer MoS₂. More importantly, compared with the 0L case (Fig. 2h), the interlayer r^2 in the 2L case is greatly suppressed to almost zero due to the largely reduced α (Fig. 2i), consistent with the mechanism proposed in Fig. 2a. Therefore, via 2Δ engineering, we may strongly enhance (suppress) the interlayer BOTs for hetero-bilayer (homo-bilayer) TMDs, yielding the corresponding enhancement (suppression) in its low energy adsorption spectroscopy (see Supplemental Fig. 4).

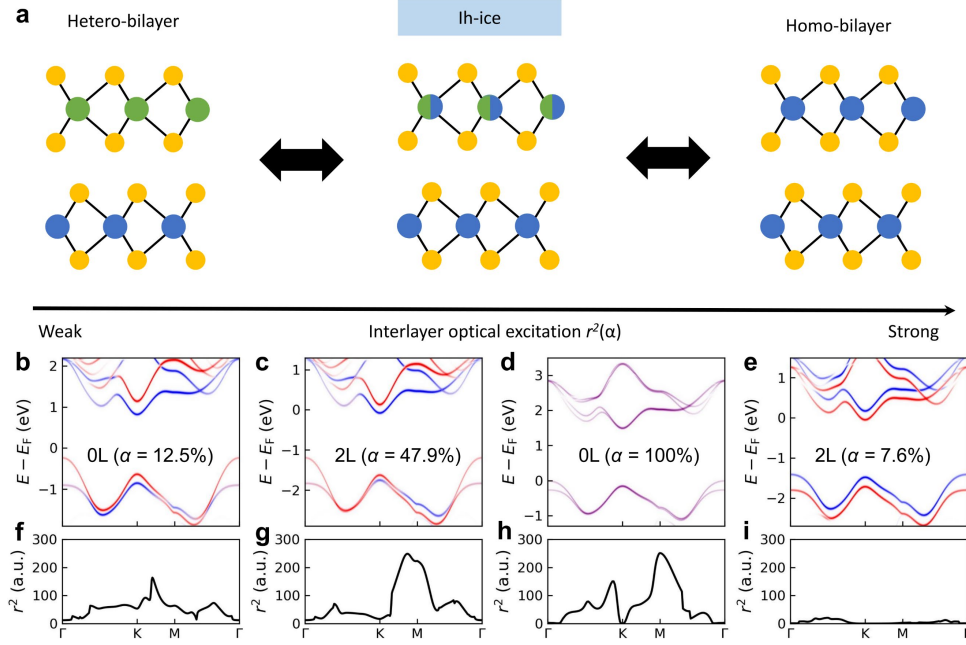


Fig.2 Optoelectronic engineering in TMD bilayers. (a) Schematic diagram of tuning interlayer optical transition probabilities (r^2) in TMD bilayers. Interlayer r^2 in TMD hetero- and homo-bilayers are weak and strong, respectively. Via 2Δ engineering, the interlayer $r^2(\alpha)$ of hetero- and homo-bilayers can be greatly enhanced and weakened, respectively. Orbital-resolved effective band structures of WS₂/MoS₂ covered by (b) 0L and (c) 2L Ih-ice. Electronic states of top WS₂ and bottom MoS₂ layers are highlighted by red and blue colors, respectively. (d)-(e) Same as (b)-(c) but for the cases of MoS₂/MoS₂. Electronic states of top and bottom MoS₂ layers are highlighted by blue and red colors, respectively. (f)-(g) Calculated interlayer r^2 between four band-edge states in the band structures of WS₂/MoS₂ shown in (b)-(c), respectively. (h)-(i) Same as (f)-(g) but for the case of MoS₂/MoS₂.

Case II: Switchable different types of Dirac fermions in Bi₂Se₃ thin films

Topological materials, starting from topological insulators (TIs), are standing in the cutting edge of quantum materials²⁰⁻²². An ideal TI, e.g., Bi₂Se₃, is a quantum matter with a bulk gap and an odd number of relativistic Dirac fermions on the surface, in which the bulk is insulating but the surface can conduct electric current with helical spin texture^{23,24}. However, it is known that Dirac surface states can only be realized in a thick Bi₂Se₃, i.e., more than six quintuple-layer (QL). Once the thickness of Bi₂Se₃ is less than six QL, the IH between the top and bottom Dirac surface states can induce a hybridization gap (Fig. 3a, left and middle panels), destroying the massless feature of Dirac surface states^{25,26}. As shown in Fig. 1b, via 2Δ engineering, we may reduce the α in Bi₂Se₃ ultrathin films, which may lift the coupling between top and bottom surface states (Fig. 3a, right-panel) and result in a transition from massive to massless Dirac fermions.

To verify this idea, as shown in Fig. 3b, we have selected 3QL-Bi₂Se₃ ultrathin films as an example, in which the top of 3QL-Bi₂Se₃ is covered by an Ih-ice overlayer. In the ice-free case (0L), $2\Delta = 0$, therefore, $\alpha = 100\%$. The hybridization between the top and bottom Dirac surface states in 3QL-Bi₂Se₃ can induce a large hybridization gap of about 50 meV between them, transforming the

original massless Dirac fermions to massive ones²⁵. Moreover, because of the effective surface-state coupling, the spin texture of massive Dirac surface states, which are completely degenerate in energy space, is far away from the ideal helical one (inset of Fig. 3c), i.e., the directions of the spin moments are not perpendicular to that of the crystal momenta.

When a 2L Ih-ice overlayer is deposited on the top of 3QL-Bi₂Se₃ slab (see Supplemental Fig. 5), it can result in $2\Delta = 239$ meV, which can consequently reduce α from 100% to almost 0%. As a result, the surface states from top and bottom layers are no longer degenerate in energy space. And the Dirac fermions on the top and bottom surfaces are restored to be massless. Interestingly, the spin textures of the Dirac surface states, which are fully separated in the energy space, are also restored to the ideally helical one, i.e., the directions of the spin moments are rigorously perpendicular to that of the crystal momenta. Therefore, an interesting transition from massive to massless Dirac fermions can be well achieved by 2Δ engineering, along with the modulation of its spin texture.

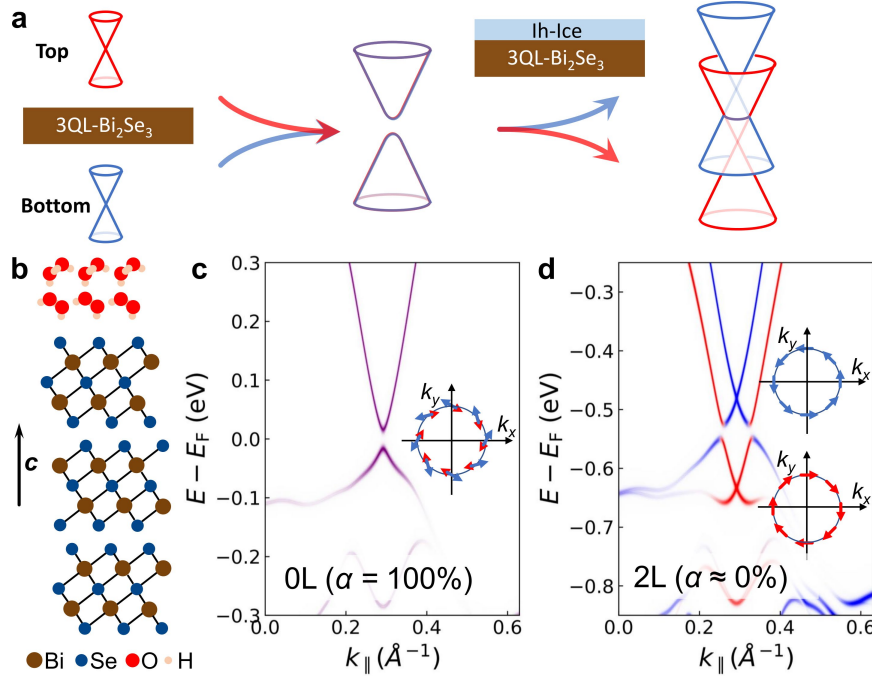


Fig. 3 Dirac surface states engineering in Bi₂Se₃ thin films. (a) Schematic diagram of switchable massive-massless Dirac fermions in 3QL-Bi₂Se₃. Because of the strong orbital hybridization, the surface states of 3QL-Bi₂Se₃ open a gap and Dirac fermions are massive (left panel to middle panel). By depositing the Ih-ice overlayer, this hybridization is expected to be effectively reduced, thus, the surface Dirac fermions will be recovered to be massless (middle panel to right panel). (b) Side view of atomic structure of 3QL-Bi₂Se₃ covered by 2L Ih-ice. Orbital-resolved effective band structure of 3QL-Bi₂Se₃ with (c) 0L and (d) 2L Ih-ice overlayer. Weights of the surface states from the top and bottom sides are highlighted by red and blue colors, respectively. Insets: spin textures of the surface states from top (red arrow) and bottom (blue arrow) sides. Shift of the surface states to lower energies in (d) results from the charge transfer from the Ih-ice overlayer to the Bi₂Se₃ (see Supplemental Fig. 6).

Case III: Controllable magnetic phase transition of CDW in 1T/1H-TaS₂

Magnetism is one of the central phenomena in condensed matter physics, which is mainly determined by the spin exchange interaction J in the system. The realization of controllable J is the key to realize controllable magnetic phase transition. A 1T/1H-TaS₂ heterostructure has recently been proposed to be a promising platform to simulate a Kondo lattice^{27,28}. The 1T-TaS₂ in the Star-of-David (SoD) charge-density wave (CDW) phase naturally forms a large unit cell with a single localized spin moment. These localized spin moments can interact with each other through the $5d$ conduction electrons in metallic 1H-TaS₂ via the IH. Thus, the J between localized spin moments and conduction electrons highly depends on α , i.e., J is a function of α (Fig. 4a). By 2Δ engineering, we may effectively control $J(\alpha)$ in 1T/1H-TaS₂, which can consequently control the magnetic phase transition of CDW in 1T/1H-TaS₂.

To verify this idea and to model the 1T/1H-TaS₂ heterostructure with the SoD-CDW phase, we combine a $\sqrt{39} \times \sqrt{39}$ 1T-TaS₂ structure with a 6×6 1H-TaS₂ structure (see Supplemental Fig. 7). The calculated local spin moment on the Ta atom in the center each SoD cluster is about $0.2 \mu_B$, and its direction can be flipped freely (there is an energy barrier of about 0.02 meV per SoD cluster), which results in a paramagnetic phase. As shown in Fig. 4b, the calculated density of states (DOS) indicates that the half-occupied state contributed by the Ta- d_{z^2} in the center of SoD in 1T-TaS₂ is pushed upwards to higher energies, while the states derived from the Ta- d in 1H-TaS₂ are pushed downwards to lower energies. This noticeable level repulsion between 1T and 1H layers around the Fermi level manifests the existence of an unignorable IH, as also indicated by the calculated $\alpha = 13.9\%$. Considering both the spin-polarization and DOS calculations, it can be concluded that the 1T/1H-TaS₂ heterostructure probably falls into the Kondo screened regime in the phase diagram in Fig.4c, consistent with the experimental observations²⁸.

If 2L Ih-ice is deposited on top of the 1T-TaS₂ layer, the increased 2Δ can weaken α . Interestingly, as shown in Fig. 4b, although α is slightly reduced from 13.9% to 10.2%, it can strongly suppress the level repulsion between the 1T- and 1H-TaS₂ layer. Instead, the Kondo spin screening of the local moments will be dominated by the RKKY interaction²⁹, leading to a magnetic order. Indeed, with the assistance of Ih-ice overlayer, the freely flipped localized spin moment in the 1T-TaS₂ layer becomes magnetically ordered with the local magnetic moment of the center Ta in each SoD cluster being of about $0.3 \mu_B$ (left in Fig. 4c). During the self-consistent iterations, all the different initial magnetic configurations will eventually converge to a collective order (left in Fig.4c), indicating a (strong) local energy minimum. Thus, a novel magnetic phase transition of CDW in the 1T/1H-TaS₂ heterostructure can be well controlled by 2Δ engineering.

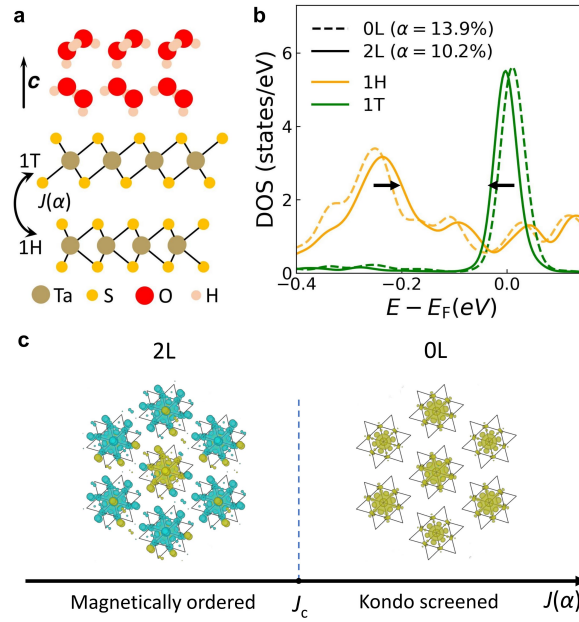


Fig. 4 Engineering magnetic phase transition in 1T/1H-TaS₂ heterostructure. (a) Side view of atomic structure of 1T/1H-TaS₂, where the top of the 1T layer is covered by Ih-ice. J is a function of α . **(b).** Projected DOS of 1T/1H-TaS₂ with 0L (dashed line) and 2L (solid line) Ih-ice overlayer. The projection on d_{z^2} orbital of the central Ta in the SoD of the 1T-TaS₂ layer is highlighted by green color, while the projection on the d_{z^2} , d_{xy} , and $d_{x^2-y^2}$ orbitals of Ta in the 1H layer is highlighted by orange color. **(c).** Schematic diagram of the magnetic phase transition between a magnetically ordered phase induced by RKKY interaction and a paramagnetic phase resulting from the Kondo screening. Left and right panel shows the calculated spin density maps of the 1T/1H-TaS₂ heterostructure with 2L and 0L Ih-ice overlayer, respectively.

Discussion

The critical factor of the IH engineering in energy space proposed here is to find a feasible approach to strongly reshape the local electrostatic potential of a surface layer. In principle, candidates for the dipole overlayers can generally be any materials with a net dipole moment perpendicular to the surface. The choice of an Ih-ice overlayer in this work is based on two concerns. First, the water molecules possess a large dipole moment (1.8-3.0 Debye)³⁰, being capable of sharply tailoring the surface electrostatic potential. Second, water molecules can be frozen into a crystalline phase with its polarization controlled by external fields³¹⁻³³. Although there are reports on polar molecules as adsorbates influencing the electronic structures of solid surfaces³⁴⁻³⁷, the adsorbate-induced variations in the IH admixture ratio is barely explored and poorly understood.

In summary, beyond the common belief that IH is mostly associated with the wavefunction overlap in real space t , we propose that IH can also be dramatically engineered in energy space by tuning the energy separation 2Δ . Via the proposed 2Δ engineering, we demonstrate that the optoelectronic, topological, and magnetic properties of different 2D vdW homo/hetero-junctions can be well modulated. Our concept and material demonstrations may open the way for new ideas for the IH engineering in vdW systems beyond the conventional ways.

Methods

Computational details

For the density-functional theory (DFT) calculations, we use the Vienna Ab Initio Simulation Package (VASP)³⁸ with the projector-augmented-wave basis sets^{39,40} and the generalized gradient approximation (GGA) to the exchange-correlation potential⁴¹. While the lattice constants of 1H-MoS₂, 1H-WS₂, 1T-TaS₂, and 1H-TaS₂ are fully optimized, the crystal structure of Bi₂Se₃ is taken from Ref. 42. To obtain a commensurate structure, we construct slabs of a $\sqrt{3} \times \sqrt{3}$ supercell of Ih-ice overlayer on a $\sqrt{7} \times \sqrt{7}$ supercell of MoS₂/MoS₂ (MoS₂/WS₂), a 1×1 Ih-ice overlayer on a 1×1 3QL-Bi₂Se₃, a $\sqrt{21} \times \sqrt{21}$ supercell of Ih-ice overlayer on a $\sqrt{39} \times \sqrt{39}$ supercell of bilayer 1T-TaS₂ on a 6×6 supercell of 1H-TaS₂, where the Ih-ice overlayers are laterally compressed or expanded to eliminate the lattice mismatch. The in-plane lattice constant of the 1T/1H-TaS₂ supercell is set to be the average value of the $\sqrt{39} \times \sqrt{39}$ supercell of 1T-TaS₂ and the 6×6 1H-TaS₂. A vacuum separation of more than 15 Å is used in all the slabs. In all the cases, the structures are relaxed until the forces acting on them are below 0.01 eV Å⁻¹. In the evaluation of the electronic structures, we choose a plane-wave cut-off energy of 400 eV for all the cases and a Γ -centered $7 \times 7 \times 1$, $15 \times 15 \times 1$, and $5 \times 5 \times 1$ k -mesh for the MoS₂/MoS₂ (MoS₂/WS₂), 3QL-Bi₂Se₃, and 1T/1H-TaS₂ case, respectively. The convergence criterion for the total energy is a change of less than 10⁻⁵ eV between self-consistency iterations. We have taken into account the vdW interaction via the D2 method of Grimme⁴³ in all the calculations, and we have applied a dipole correction⁴⁴ in the direction perpendicular to the slab in the cases with Ih-ice overlayer. The spin-orbit coupling is included in the calculation of the surface state and the spin texture of 3QL-Bi₂Se₃. The $+U$ correction⁴⁵ with $U - J = 2.27$ eV^{46,47} has been applied to the Ta- d orbital in the 1T layer.

Effective Wannier Hamiltonian

We construct an effective Hamiltonian in the basis of atomic projected Wannier functions in the MoS₂/MoS₂, MoS₂/WS₂, and 3QL-Bi₂Se₃ cases using the Wannier90 package⁴⁸, see Supplemental Figs. 8, 9 and 10. We choose the W- d , Mo- d , and S- p orbitals of MoS₂ and WS₂, O- p orbitals of the Ih-ice, and Bi- p and Se- p orbitals of Bi₂Se₃ as initial projections in the disentanglement process. In the case of the TMD bilayers, the effective Hamiltonian of the supercell is further mapped to the TMD primitive cell using our developed routines in the elphmod package⁴⁹. Here, the exact choice of the primitive cell does not have a noticeable influence on the resulting band structure, showing that the change of the onsite energy differences 2Δ due to the Ih-ice overlayer is homogeneous.

Estimation of the admixture ratio α

For the case of MoS₂/MoS₂, MoS₂/WS₂, and 3QL-Bi₂Se₃, we estimate the corresponding admixture ratio α from the expression $\alpha = 1 - 1/\sqrt{1 + 4(t/2\Delta)^2}$. We choose the parameter t as the leading term of the nearest-neighbour hopping between the orbitals from different layers, which are $\{\text{Mo/W-}d_{z^2}^{\text{top}}, \text{Mo-}d_{z^2}^{\text{bottom}}\}$ and $\{\text{Bi-}p_z^{\text{top}}, \text{Bi-}p_z^{\text{bottom}}\}$ in the case of MoS₂/MoS₂ (WS₂/MoS₂) and 3QL-Bi₂Se₃, respectively. The parameter 2Δ is obtained as the difference of the onsite energies between corresponding orbitals. Given the large number of atoms in the 1T/1H-TaS₂ system, we select an alternative way of estimating the admixture ratio α for computational feasibility. We integrate the density of states projected on the d_{z^2} orbital of the Ta atom in the center of SoD cluster (Ta^{SoD}- d_{z^2}) and on the d_{z^2} orbital of its nearest neighbor Ta atom in the 1H layer. The integration energy window is determined by the full width at half maximum of the Ta^{SoD}- d_{z^2} peak.

The admixture ratio α is then calculated as $\alpha = 1 - |N^{1T} - N^{1H}|/(N^{1T} + N^{1H})$, where N^{1T} and N^{1H} are the integrated projected densities of states.

Calculation of the optical transition dipole moments (TDMs)

The effective Wannier Hamiltonians of the primitive cell of the TMD bilayers and their eigenfunctions are applied to calculate the band velocity v_{nm} with $v_{nm} = \langle n, k | \partial_k H | m, k \rangle$ where n, m are electronic band indices. To identify the interlayer contributions to the band velocity, we introduce the project operator by following $v_{gg'}^{\text{Inter}} = \langle g, k | \partial_k H | g', k \rangle = \sum_{n,m} \langle g, k | n, k \rangle \langle n, k | \partial_k H | m, k \rangle \langle m, k | g', k \rangle$, where the local orbitals $|g, k\rangle, |g', k\rangle$ belong to different layers. The TDMs r_{nm} can be obtained with the relation $r_{nm} = v_{nm}/i\omega_{nm}$ ($m \neq n$), where ω_{nm} is the eigenvalue difference between $|n, k\rangle$ and $|m, k\rangle$. Here, the estimated r^2 (squares of TDMs) are the sum of four optical transition processes between the top two valence bands and the bottom two conduction bands. These calculations are performed in our homemade NOPSS package⁵⁰.

Calculation of orbital-resolved effective band structures

Using the effective Wannier Hamiltonian, we calculate the interpolated band structure $\epsilon_n(k)$ and its Bloch state $|n, k\rangle$ in the cases of MoS₂/MoS₂, MoS₂/WS₂, and 3QL-Bi₂Se₃. Then, we estimate the orbital-resolved effective band structure via the spectral function $A(\omega, k)$ on a localized orbital

$|g, k\rangle$ defined as $A^g(\omega, k) = -2\text{Im} \frac{\langle n, k | g, k \rangle \langle g, k | n, k \rangle}{\omega - \epsilon_n(k) + i0^+}$, where $i0^+$ is an imaginary offset.

Acknowledgements

We acknowledge the support from the NSFC (No. 12088101), the NSAF (No. U1930402). J. B. acknowledges the financial support by the Deutsche Forschungsgemeinschaft (DFG) through EXC 2077. We acknowledge Drs. Wujun Shi, Fawei Zheng, and Tim Wehling for fruitful discussions. The calculations were performed at Tianhe2-JK at CSRC.

References

1. Geim, A. K. & Grigorieva, I. V. Van der Waals heterostructures. *Nature* **499**, 419–425 (2013).
2. Novoselov, K. S., Mishchenko, A., Carvalho, A. & Castro Neto, A. H. 2D materials and van der Waals heterostructures. *Science* **353**, aac9439 (2016).
3. Cappelluti, E., Roldán, R., Silva-Guillén, J. A., Ordejón, P. & Guinea, F. Tight-binding model and direct-gap/indirect-gap transition in single-layer and multilayer MoS₂. *Phys. Rev. B* **88**, 075409 (2013).
4. Tongay, S. *et al.* Tuning Interlayer Coupling in Large-Area Heterostructures with CVD-Grown MoS₂ and WS₂ Monolayers. *Nano Lett.* **14**, 3185–3190 (2014).
5. Fang, H. *et al.* Strong interlayer coupling in van der Waals heterostructures built from single-layer chalcogenides. *Proc. Natl. Acad. Sci.* **111**, 6198–6202 (2014).
6. Xia, J. *et al.* Strong coupling and pressure engineering in WSe₂–MoSe₂ heterobilayers. *Nat. Phys.* **17**, 92–98 (2021).
7. Novoselov, K. S. *et al.* Electric Field Effect in Atomically Thin Carbon Films. *Science* **306**, 666–669 (2004).
8. Hunt, B. *et al.* Massive Dirac Fermions and Hofstadter Butterfly in a van der Waals

- Heterostructure. *Science* **340**, 1427–1430 (2013).
9. Li, T. *et al.* Pressure-controlled interlayer magnetism in atomically thin CrI₃. *Nat. Mater.* **18**, 1303–1308 (2019).
 10. Song, T. *et al.* Switching 2D magnetic states via pressure tuning of layer stacking. *Nat. Mater.* **18**, 1298–1302 (2019).
 11. Zhou, H., Xie, T., Taniguchi, T., Watanabe, K. & Young, A. F. Superconductivity in rhombohedral trilayer graphene. *Nature* **598**, 434–438 (2021).
 12. Rivera, P. *et al.* Observation of long-lived interlayer excitons in monolayer MoSe₂–WSe₂ heterostructures. *Nat. Commun.* **6**, 6242 (2015).
 13. Rivera, P. *et al.* Valley-polarized exciton dynamics in a 2D semiconductor heterostructure. *Science* **351**, 688–691 (2016).
 14. Ritschel, T. *et al.* Orbital textures and charge density waves in transition metal dichalcogenides. *Nat. Phys.* **11**, 328–331 (2015).
 15. Butler, C. J., Yoshida, M., Hanaguri, T. & Iwasa, Y. Mottness versus unit-cell doubling as the driver of the insulating state in 1T-TaS₂. *Nat. Commun.* **11**, 2477 (2020).
 16. Cao, Y. *et al.* Unconventional superconductivity in magic-angle graphene superlattices. *Nature* **556**, 43–50 (2018).
 17. Cao, Y. *et al.* Correlated insulator behaviour at half-filling in magic-angle graphene superlattices. *Nature* **556**, 80–84 (2018).
 18. Brill, R. & Tippe, A. Gitterparameter von Eis I bei tiefen Temperaturen. *Acta Crystallogr.* **23**, 343–345 (1967).
 19. Hong, X. *et al.* Ultrafast charge transfer in atomically thin MoS₂/WS₂ heterostructures. *Nat. Nanotechnol.* **9**, 682–686 (2014).
 20. Fu, L., Kane, C. L. & Mele, E. J. Topological Insulators in Three Dimensions. *Phys. Rev. Lett.* **98**, 106803 (2007).
 21. Hasan, M. Z. & Kane, C. L. *Colloquium* : Topological insulators. *Rev. Mod. Phys.* **82**, 3045–3067 (2010).
 22. Qi, X.-L. & Zhang, S.-C. Topological insulators and superconductors. *Rev. Mod. Phys.* **83**, 1057–1110 (2011).
 23. Zhang, H. *et al.* Topological insulators in Bi₂Se₃, Bi₂Te₃ and Sb₂Te₃ with a single Dirac cone on the surface. *Nat. Phys.* **5**, 438–442 (2009).
 24. Xia, Y. *et al.* Observation of a large-gap topological-insulator class with a single Dirac cone on the surface. *Nat. Phys.* **5**, 398–402 (2009).
 25. Lu, H.-Z., Shan, W.-Y., Yao, W., Niu, Q. & Shen, S.-Q. Massive Dirac fermions and spin physics in an ultrathin film of topological insulator. *Phys. Rev. B* **81**, 115407 (2010).
 26. Zhang, Y. *et al.* Crossover of the three-dimensional topological insulator Bi₂Se₃ to the two-dimensional limit. *Nat. Phys.* **6**, 584–588 (2010).
 27. Chen, C., Sodemann, I. & Lee, P. A. Competition of spinon Fermi surface and heavy Fermi liquid states from the periodic Anderson to the Hubbard model. *Phys. Rev. B* **103**, 085128 (2021).
 28. Vaño, V. *et al.* Artificial heavy fermions in a van der Waals heterostructure. *Nature* **599**, 582–586 (2021).
 29. Doniach, S. The Kondo lattice and weak antiferromagnetism. *Phys. BC* **91**, 231–234 (1977).
 30. Dyke, T. R. & Muenter, J. S. Electric dipole moments of low *J* states of H₂O and D₂O. *J. Chem. Phys.* **59**, 3125–3127 (1973).

31. Svishchev, I. M. & Kusalik, P. G. Crystallization of Liquid Water in a Molecular Dynamics Simulation. *Phys. Rev. Lett.* **73**, 975–978 (1994).
32. Svishchev, I. M. & Kusalik, P. G. Electrofreezing of Liquid Water: A Microscopic Perspective. *J. Am. Chem. Soc.* **118**, 649–654 (1996).
33. Sutmann, G. Structure formation and dynamics of water in strong external electric fields. *J. Electroanal. Chem.* **450**, 289–302 (1998).
34. Karschnick, G., Anderson, O., Drube, W. & Skibowski, M. Adsorbate enhanced Ti-3d photoemission from layered TiSe₂ surfaces. *Surf. Sci.* **155**, 46–52 (1985).
35. Rasch, J. C. E., Stemmler, T., Müller, B., Dudy, L. & Manzke, R. 1T-TiSe₂: Semimetal or Semiconductor? *Phys. Rev. Lett.* **101**, 237602 (2008).
36. May, M. M., Brabetz, C., Janowitz, C. & Manzke, R. Charge-Density-Wave Phase of 1T-TiSe₂: The Influence of Conduction Band Population. *Phys. Rev. Lett.* **107**, 176405 (2011).
37. Shen, S. *et al.* Single-water-dipole-layer-driven Reversible Charge Order Transition in 1T-TaS₂. *Nano Lett.* **20**, 8854–8860 (2020).
38. Kresse, G. & Hafner, J. Norm-conserving and ultrasoft pseudopotentials for first-row and transition elements. *J Phys Condes Matter* **6**, 8245–8257 (1994).
39. Blöchl, P. E. Projector augmented-wave method. *Phys. Rev. B* **50**, 17953–17979 (1994).
40. Kresse, G. & Joubert, D. From ultrasoft pseudopotentials to the projector augmented-wave method. *Phys. Rev. B* **59**, 1758–1775 (1999).
41. Perdew, J. P., Burke, K. & Ernzerhof, M. Generalized Gradient Approximation Made Simple. *Phys Rev Lett* **77**, 3865–3868 (1996).
42. Zhang, W., Yu, R., Zhang, H.-J., Dai, X. & Fang, Z. First-principles studies of the three-dimensional strong topological insulators Bi₂Te₃, Bi₂Se₃ and Sb₂Te₃. *New J. Phys.* **12**, 065013 (2010).
43. Grimme, S. Semiempirical GGA-type density functional constructed with a long-range dispersion correction. *J. Comput. Chem.* **27**, 1787–1799 (2006).
44. Neugebauer, J. & Scheffler, M. Adsorbate-substrate and adsorbate-adsorbate interactions of Na and K adlayers on Al(111). *Phys. Rev. B* **46**, 16067–16080 (1992).
45. Dudarev, S. L., Botton, G. A., Savrasov, S. Y., Humphreys, C. J. & Sutton, A. P. Electron-energy-loss spectra and the structural stability of nickel oxide: An LSDA+*U* study. *Phys. Rev. B* **57**, 1505–1509 (1998).
46. Darancet, P., Millis, A. J. & Marianetti, C. A. Three-dimensional metallic and two-dimensional insulating behavior in octahedral tantalum dichalcogenides. *Phys. Rev. B* **90**, 045134 (2014).
47. Qiao, S. *et al.* Mottness Collapse in 1T-TaS_{2-x}Se_x Transition-Metal Dichalcogenide: An Interplay between Localized and Itinerant Orbitals. *Phys. Rev. X* **7**, 041054 (2017).
48. Pizzi, G. *et al.* Wannier90 as a community code: new features and applications. *J. Phys. Condens. Matter* **32**, 165902 (2020).
49. Berges, J., Schobert, A., van Loon, E. G. C. P., Rösner, M. & Wehling, T. O. *elphmod: Python modules to handle electron-phonon models (v0.10)*. (Zenodo, 2022). doi:10.5281/zenodo.5919992.
50. Jiang, X., Kang, L. & Huang, B. Role of interlayer coupling in second harmonic generation in bilayer transition metal dichalcogenides. *Phys. Rev. B* **105**, 045415 (2022).